Nuclear Science and Techniques (2025) 36:60
https://doi.org/10.1007/s41365-025-01638-y

Compact RF linear accelerator for electron beam irradiation applications at PBP-CMU Electron Linac Laboratory

Monchai Jitvisate[1,4] · **Pittaya Apiwattanakul**[1] · **Noppadol Kangrang**[1,2] · **Jatuporn Saisut**[1,2,3] · **Chitrlada Thongbai**[1,2,3] · **Sakhorn Rimjaem**[1,2,3]

Received: 8 September 2023 / Revised: 9 April 2024 / Accepted: 20 May 2024 / Published online: 23 February 2025

Abstract
A 4 MeV RF linear accelerator for electron beam irradiation applications has been developed at the PBP-CMU Electron Linac Laboratory, Thailand. The system has been reengineered using a decommissioned medical linear accelerator. The main components include a thermionic DC electron gun, an RF linear accelerator, a beam diagnostic chamber, and a beam exit window for electron beam irradiation. Therefore, reengineering must be performed based on the characteristics of the electron beam and its dynamics throughout the system. In this study, the electron beam current density emitted from the cathode was calculated based on the thermionic emission theory, and the result was used to produce the electron beam distribution in the gun using CST Studio Suite® software. The properties of the electron beam and its acceleration in the linear accelerator and downstream diagnostic section were studied using the ASTRA electron beam dynamics simulation code, with the aim of producing an electron beam with an average energy of 4 MeV at the linear accelerator exit. The transverse beam profile and electron deposition dose in the ambient environment were calculated using Geant4 Monte Carlo simulation software to estimate the beam performance for the irradiation experiments. The parameters studied can be used as guidelines for machine operation and future experimental plans.

Keywords Thermionic electron gun · RF linear accelerator · Electron dynamics simulation · Monte Carlo simulation · Electron beam irradiation · Electron beam processing · Deposition dose

1 Introduction

Over many decades, electron beams have proved to be a powerful technique for various applications, from material studies and modifications to food quality control [1–6]. The fundamental mechanism behind this success, like other ionizing radiations (e.g., X-rays and gamma rays), is the breaking and reforming of chemical bonds in materials caused by energetic particles [7]. Several applications utilize electron beam irradiation, but the vast majority involve polymer modification and processing [7–13]. The main reason for this is that many properties of polymers can be altered by changing their chain lengths and molar masses. Electron beams are perfectly capable of scission and cross-linking in polymers without the use of chemicals, thereby providing residue-free materials [2, 7, 9, 14]. Even when additives or sensitizers are required, the initiation of reactions also benefits from prior physical bond damage caused by electron irradiation [7, 15]. The ionization process caused by energetic electron beams can modify material properties in polymers as well as other materials such as carbon nanomaterials [5, 16–18]. There have been reports on changes in the thermal and electrical properties of graphene and carbon nanotubes owing to defects and dislocations produced by electron beams, which can have promising consequences for field effect and nanodevice research [5, 19–21]. Another interesting effect of electron beam rather than the "breaking" ability is "jointing" behavior, which facilitates the manipulation nanostructures. Clear evidence from the literature is carbon nanotube

This work was supported by Chiang Mai University for providing infrastructure and the NSRF via the Program Management Unit for Human Resources & Institutional Development, Research and Innovation [grant number B05F650022] for the software CST Studio Suite® 2023. Financial support for the reengineering and commissioning of the accelerator system was provided by the Thailand Center of Excellence in Physics (ThEP Center) and Science and Technology Park Chiang Mai University (CMU STeP).

Extended author information available on the last page of the article

welding using electron beam irradiation, which has been studied both computationally and experimentally [5, 22–24].

Apart from laboratory-scale research, electron beam technology has also been used in different industries, for example, decontamination and disinfection of food and agricultural products and natural rubber vulcanization [6, 25–28]. Such large-scale use can have a significant impact on society in terms of both quality improvement and economics. To promote research in these relevant fields and conduct these industrial activities, an energetic electron source is a "necessary condition". However, in contrast to radioactive radiation, the production of energetic electrons requires particle accelerators (specifically, electron accelerators), which are expensive and require specialized workers. Consequently, investments in this type of research and industry always face uncompromising considerations, particularly in many developing countries.

In Thailand, certain number of electron accelerators are in operation. However, most of them are housed in hospitals and used mainly for medical purposes. The use of electron accelerators in scientific research and industry is still scarce and limited to only a few facilities, such as national laboratories. Therefore, research in the field of electron beam irradiation is quite quiescent because of the difficulty in accessing this technique. Consequently, the transfer of technology to industry is even more difficult to promote. This limitation is primarily owing to the overall machine and service expenses as well as the lack of knowledgeable people in the field of particle accelerator physics and engineering. The in-house development of electron accelerators and experimental facilities has been considered as sustainable solution to this limitation because it can reduce the country's external expenditures (commercial machine purchase) and facilitate the education of the people working in related fields.

This paper explains the details of the reengineering and development of a research electron linear accelerator (LINAC) for electron beam irradiation applications from the old decommissioned 4 MeV medical linac. This includes technical aspects and calculations of both the machine and electron beam properties in three main sections of the system: direct current (DC) electron gun, radio frequency (RF) linac, and an additional in-house-designed irradiation station. The emission current density from the cathode surface was determined based on the measured surface temperature, with theoretical limit considerations. This was used as an important input parameter for the simulation of the electron dynamics in a gun to achieve beam properties that are more realistic than those in our previous study [29]. The electron beam exiting the gun was then used as an input for the study of the electron beam dynamics in the RF linac. The extraction of the accelerated electron bunch through a vacuum window at the linac exit and the ambient beam properties, such as the transverse distribution and deposition dose along the travel distance, were then studied using a simulation based on the Monte Carlo method. The results presented in this study are expected to serve as important guidelines for future commissioning activities such as electron beam characterization, electron beam extraction, dose measurement, and beam irradiation experimental design.

2 Description of the accelerator system

Our accelerator system was reengineered based on two major components (an electron gun and accelerating structure) retrieved from a decommissioned medical linac (Model ML-4 M, Mitsubishi Electric, Japan) [30]. The original model was designed to achieve a final electron kinetic energy of up to approximately 4 MeV to produce X-rays. The reengineered accelerator system is used for electron beam irradiation. Therefore, certain parts were modified and added. The tungsten target at the linac end was removed, and a diagnostic chamber was installed. A titanium window was attached to the end of the chamber to extract the electron beam. A schematic of the system is shown in Fig. 1. The technical details of each component are described in the following sections.

2.1 The electron gun

The electron gun is the starting section of the accelerator system and provides electrons for the accelerating structure. It comprised two main parts: an emission electrode (cathode) and an extraction electrode (anode). The cathode is a source of electrons for accelerator systems and is typically composed of low-work-function materials to obtain a high electron yield. The cathode used in our system released electrons via thermionic emission. An impregnated dispenser tungsten cathode (Model 532; HeatWave Labs, CA, USA) was used. The temperature-dependent work function (W) of this cathode, as quoted by the manufacturer, was $1.67 + (3.17 \times e^{-4})T$ eV, where T is the absolute temperature [31]. The cathode had a circular flat surface with a diameter of 4.86 mm. It was housed in a cathode assembly connected to an electron gun, as shown in Fig. 1. The estimated heating condition was quoted at a voltage of 2.7 VAC and current of 16 A [30]. As the electrical power increased, the temperature of the cathode surface increased, emitting both electrons and photons. The important properties of the cathode are described in Sect. 3.1.

The electron gun in our system was a Pierce-type DC gun with copper electrodes (cathode and anode) and using stainless steel as the gun housing. The anode, which also acted as a focusing electrode, was located 9 mm away from the cathode surface (Fig. 1). It was originally designed to achieve a maximum DC extraction voltage of 17 kV [30]. This value

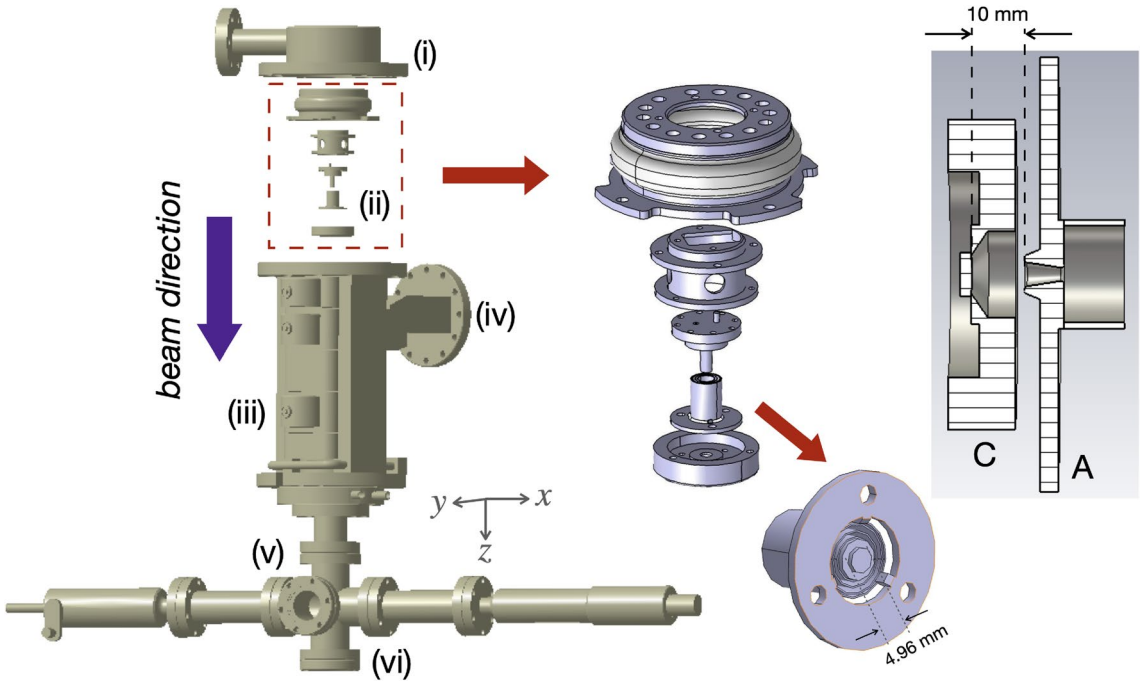

Fig. 1 Schematic of system components: (i) electron gun, (ii) cathode assembly with enlarged cathode structure, (iii) linac, (iv) feed-in RF waveguide, (v) diagnostic chamber, and (vi) beam exit. On the right-hand side is the schematic of the gun's cross section showing cathode (C) and anode (A) configuration. The structures are drawn according to actual dimension measurement

was used throughout the study, unless stated otherwise. The vacuum duct was connected to the sidewall of the gun and directed to an ion pump to maintain high vacuum inside the gun. The gun emission current was determined by the vacuum pressure, heating power of the cathode, and extraction voltage of the anode.

2.2 The accelerating structure

A linac is an accelerating structure wherein an electron beam gains kinetic energy through acceleration in an electric field. The linac structure is illustrated in Part iii of Fig. 1. The entire piece was made of copper with five TM_{010}-mode standing-wave resonant cavities and side-coupling cavities. It was originally designed to accelerate electrons in the $\pi/2$ mode with a final average electron kinetic energy of 4 MeV [30]. In our reengineered system, an adjustable variac transformer was added to vary the high voltage of the RF system. Consequently, the electron beam energy could be adjusted according to the RF power [30]. The RF field in accelerator cavities was a standing-wave electric field formed by the superposition of forward and backward waves. The RF phase inside the consecutive cavities differed by π, whereas that inside the side-coupling cavities differed by $\pi/2$ with respect to the main accelerating cavities. These side cavities produced a node of the standing wave and maintained a zero electric field. The RF wave was generated from a 2-MW magnetron (Model M5125), which was powered by a high-voltage power supply through a variac transformer and a pulse-forming network. By adjusting the variac, the RF peak power could be varied between 0.6 and 1.6 MW. This high-power RF wave was then fed to the linac through a WR-284 rectangular copper waveguide (Part iv of Fig. 1), which was filled with sulfur hexafluoride (SF_6) gas to prevent arcing. This pressurized section was separated from the vacuum of the linac using a ceramic RF window. Inside the linac, the RF wave was coupled between the resonant cavities through side-coupling cavities. The forward and reflected RF powers were measured using a directional coupler located in front of the ceramic window.

2.3 Beam characterization section and experimental station

This accelerator was originally been designed by the manufacturer to produce X-rays for medical purposes [30]. Therefore, the original linac end was enclosed by a tungsten target and a lead equalizer. To utilize an energetic electron beam, this end section must be modified such that the accelerated electrons can exit the ambient environment. Thus, we replaced the X-ray extraction section at the end of the linac with an extension tube of length 55 mm and a 6-way stainless steel cross vacuum component (Fig. 1 (v)), whose inner diameter was 38.1 mm for each pipe. Along the beam axis,

the total cross length was 130 mm; therefore, this additional section extended the beam drift space from the end of the linac, with an overall distance of 185 mm. At the final end, a 50 µm-thick titanium window was installed. This window facilitated the electron beam in penetrating the external atmospheric pressure while maintaining internal vacuum conditions ($\sim 10^{-7} - 10^{-8}$ Torr).

Perpendicular pipes were used as part of the electron beam characterization unit, or the diagnostic chamber. Two pneumatic linear motion feedthrough actuators (MDC P/N. 662006, USA) were fitted to allow installation and movement of the phosphor screen used for beam size measurement and the in-house Faraday cup for charge measurement. The actuators were moved in and out via pressurized air. The screen was composed of a 0.5 mm-thick aluminum plate coated on one side with a phosphor material (Gd_2O_2S). The screen dimensions were 28 mm × 40 mm. The beam size was observed through a glass window using the CCD camera (Basler, acA 640-120 gm with lens M7528-MP). The CCD sensor of the camera contained 659 × 659 pixels with a resolution of 5.6 µm/pixel.

Additional modifications were made to this section by installing two beam-steering magnets close to the linac end. The magnets were air coils composed of copper wires. Each coil had 255 turns and could operate without overheating in an ambient environment at maximum current and voltage of 3 A and 14 V, respectively. The magnetic field strength at 3 A was approximately 12 mT. This magnet set played an important role in beam energy measurement. The customized sample conveyer was placed a few centimeters below the titanium window. It was designed such that the sample could be placed on the conveyer and the electron dose could be varied by moving the sample passing the beam at various conveyer speeds. The details of conveyer design and study are beyond the scope of this study and will be reported elsewhere.

3 Electron beam properties and dynamics

3.1 Electron current density and dynamics in the gun

3.1.1 Cathode emission and expected current density

The current density of electrons emitted from a cathode via thermionic emission depends on the surface temperature, as explained by Richardson's law [32–34]. This current density is enhanced in the presence of an external electric field because this field lowers the work function of the materials by ΔW. This is known as the Schottky effect, and the current density can be determined using the following equation [31, 32, 35]:

$$J_R = A_0 \lambda_R T^2 e^{-(W-\Delta W)/k_B T}, \tag{1}$$

where $A_0 = 1.20173 \times 10^6$ A m^{-2} K^{-2} is the universal constant, $\lambda_R \approx 0.5$ is the correction factor for metals[36], W is the temperature-dependent work function, T is the absolute emission temperature, and k_B is the Boltzmann constant. In this expression, the field-enhanced effect yields $\Delta W = \sqrt{e^3 E/4\pi\epsilon_0}$, where e is the elementary charge, E is the electric field strength (in [V/m]), and ϵ_0 is the permittivity of free space. This thermionic electron current is then extracted using an electron gun with a potential gradient between the cathode and anode. If all emitted electrons leave the volume in front of the cathode under the influence of the applied extraction gradient, the gun is considered to be in the temperature limit regime, and the gun's current density is equal to J_R. However, if the cathode temperature is excessively high, such that an electron space charge accumulates in front of the cathode, the gun is in the space-charge limit state. In this region, the current density plateaus regardless of the heating temperature, indicating that its lifetime is shortened without producing any higher current density. Consequently, the gun's current density is limited by J_C, that is, the voltage-dependent current density, as explained by the Child–Langmuir law [32–34]:

$$J_C = \frac{4\epsilon_0}{9}\sqrt{\frac{2e}{m_e}}\frac{V_a^{3/2}}{d^2}, \tag{2}$$

where V_a is the potential difference between the two electrodes, d is the cathode–anode effective separation (9.02 mm in this study), and ϵ_0, e, and m_e are the permittivity of free space, elementary charge, and electron mass, respectively. The empirical form of the total current density J is $J^{-1} = J_R^{-1} + J_C^{-1}$[34].

Equation (1) shows that for a given material, measuring the emitted electron current density requires the determination of the absolute emission temperature, T, of the surface. A standard method involves observing the wavelength and brightness of the emitting body, and the absolute brightness temperature T_λ is determined by using a pyrometer. However, the brightness temperature is always lower than the true emission temperature, and conversion must be performed in accordance with the relation [31]

$$\frac{1}{T} = \frac{1}{T_\lambda} + \frac{\lambda \ln(\epsilon_\lambda)}{C}, \tag{3}$$

where λ is the observed optical wavelength according to the pyrometer and $C = 1.433$ cm · deg. Note that $\lambda = 650$ nm in this study.

The cathode manufacturer (HeatWave Labs, Inc.) measured cathode temperature at various heating powers using an optical pyrometer. The variation in the brightness temperature of the cathode used in our system with applied electrical

heating power is shown in Fig. 2a. By increasing the cathode heating power from approximately 15 W to 50 W, the brightness temperature obtained from the pyrometer increased from ~1120 K to ~1480 K. This measured brightness temperature was then converted to the emission temperature using Eq. (3), and exhibited slightly higher values. The expected temperature-dependent electron current density from the cathode can be calculated using Eq. (1). The results are presented in Fig. 2b together with the theoretical prediction line when the potential difference is $V_a = 17$ kV, which is the upper limit of the gun's power supply. Based on this theory, the maximum emission current calculated from our cathode temperature measurements was estimated to be approximately 885 mA, corresponding to a cathode heating power of approximately 50 W. The data also indicate that the current density was still below the space-charge limit region (plateau).

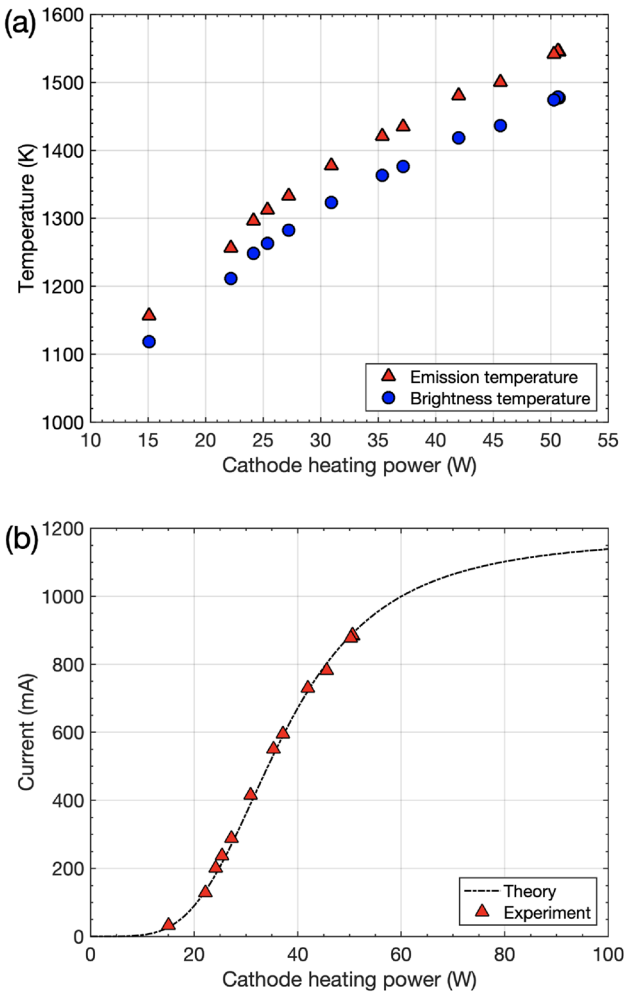

Fig. 2 **a** Measured cathode brightness temperature, T_λ, and calculated emission temperature, T, at varied heating power. **b** Calculated emission current as a function of cathode heating power. The data clearly show that the experimental current density range is still below the space-charge limit (at $V_a = 17$ kV)

3.1.2 Electron beam dynamics in the gun

To construct the electron beam for the simulation throughout the system, the emission current obtained in the previous section was used as the input for the simulation of the electron acceleration in the gun. In this study, CST Studio Suite® version 2023 [37] was used to construct the electric field inside the gun and trace the emitted electrons through the field. The electric field inside the gun structure was generated based on the potential difference between the cathode and anode of 17 keV.

Two sets of simulations were performed in the study described in this section. First, CST EM Studio software was used to create the three-dimensional (3D) model of the electron gun. The vertical cross section of the model is shown in Fig. 1. In this model, the cathode diameter was 4.96 mm, focusing electrode aperture was 4.10 mm, anode aperture was 2.10 mm, and accelerating gap was 9.02 mm. The 3D electric field distribution inside the gun structure was achieved by applying a potential difference of 17 keV between the cathode and anode. The electric field vector plot and intensity distribution are shown in Fig. 3a. A uniform electric field in the region between the cathode and anode was observed, whereas the field was stronger at a diameter greater than the anode aperture. The electric field vectors in this region were not parallel to the beam axis at the anode, which resulted in a focusing field experienced by the electron beam as it entered the anode aperture.

Second, the electron beam dynamics in the gun were simulated using CST Particle Studio software. In this simulation, electrons were tracked using the electric field distribution obtained from the simulation described in the previous paragraph. An input electron current of 885 mA was applied, which is equivalent to a current density of 4.7×10^4 A/m^2 at the cathode surface. The longitudinal cross section of the electron beam traveling from the cathode to the anode aperture is illustrated in Fig. 3b. As evident, the anode entrance is very close to the cathode and there is no focusing electrode in this DC electron gun, as in the modern design of medical linacs. Consequently, not all electrons were properly focused on the anode entrance aperture. Certain electrons hit this area, causing a dark burned area around the anode entrance, which was observed in the actual setup. The beam collision with the anode caused a significant current loss. The evolution of the corresponding RMS transverse beam size from the cathode to the linac entrance is shown in Fig. 3c. As evident, the electron beam was focused and had a minimum transverse size at the position of the linac entrance owing to the nonuniform electric field lines at the anode aperture. Beyond this position, the beam size increased slightly. The

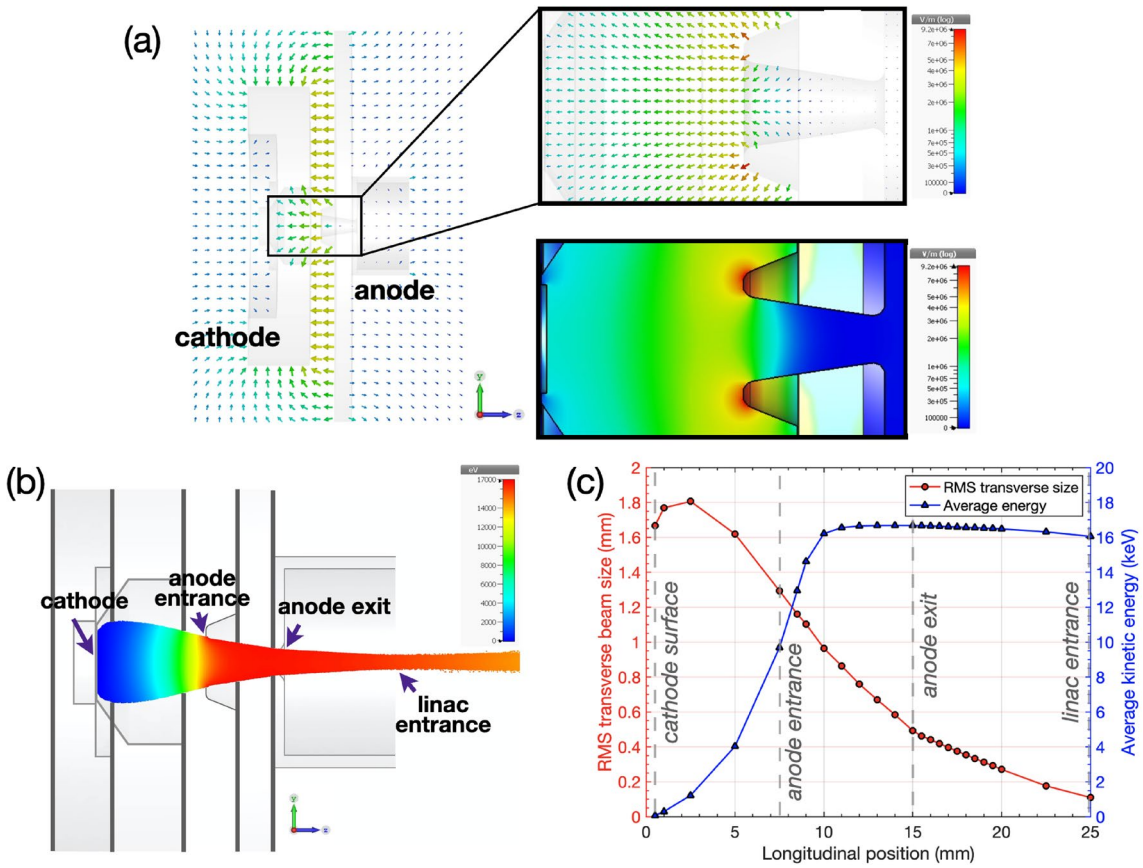

Fig. 3 **a** Simulated electric field vectors and intensity distribution (colorbar range: $0 - 9.2 \times 10^6$ V/m). **b** Longitudinal cross section of the gun and electron beam traveling from the cathode to the entrance of the linac structure (colorbar range: $0 - 17$ keV). **c** RMS transverse size and the average kinetic energy of the electron beam from the cathode surface to the linac structure

evolution of the average kinetic energy of the electron beam inside the gun is shown in Fig. 3c. An increase in the average beam energy from 0.07 keV at the cathode surface to a maximum energy of 16.7 keV at a position of 5 mm behind the anode entrance was observed. After this position, the average kinetic energy decreased slightly, and a beam with a kinetic energy of 16.0 keV was injected into the linac. The decrease in kinetic energy can be caused by the longitudinal space-charge field in the low electric field region between the anode exit and the linac entrance.

The output electron beam at the gun exit was a continuous beam containing 2,112,232 macroparticles, each with an average charge of $(3.9 \pm 0.3) \times 10^{-8}$ nC. Over a period of 333.6 ps (one RF cycle at a resonant frequency of 2996.82 MHz [27]), this resulted in a total charge of 82 ± 6 pC, corresponding to a current of 245 ± 20 mA. The transverse distribution of the electron beam was circular, with an RMS radius of 0.4 ± 0.1 mm. The beam kinetic energy calculated from the momentum of all the particles in the simulation was found to be 17.51 ± 0.01 keV. The distribution was then used as an input particle to study the electron beam dynamics in the linac. This offered an advantage over previous studies [27, 29] in that the simulated electron beam injected into the linac structure had properties and a distribution closer to the expected beam in actual operation.

3.2 Electron beam dynamics in the linac

After exiting the gun, the electron beam entered the linac section and was accelerated by the RF field. To understand the dynamics of the electron beam inside the linac, the ASTRA simulation code (DESY, Hamburg, Germany) was applied to track the trajectory of the electrons, including the space-charge interaction. To perform the simulation, all the necessary parameters associated with the real system, such as the electric field profile, electron beam distribution, and physical geometry of the beamline, must be provided.

In our system, the longitudinal electric field profile along the linac axis was measured using the bead-pull technique, as presented in our published articles [27, 29]. In this study, the same normalized field profile was applied with the maximum field gradient adjusted to 37.5 MV/m to obtain a final average beam kinetic energy of approximately 4 MeV. This value matched the optimal

design of the original system. The electron beam distribution obtained from simulations using the CST Studio Suite® software in the previous section was used as the input. The distribution included the dimensional position, 3D momentum, time, charge, type, and status of each macroparticle. As the beam was symmetric in cylindrical coordinates, a cylindrical symmetric space-charge grid was chosen. The beam direction was set along z-axis, and the beam cross section was in the $x - y$ plane. The numbers of radial and longitudinal grid rings were 50 and 100, respectively. The field plot subprogram was used in the grid verification and optimization steps. The overall simulation comprised a linac (field area) and a downstream vacuum (drift space). The limit of the field area was $z = 0 - 222.0$ mm and the downstream vacuum drift space distance was $z = 222.0 - 466.5$ mm, where $z = 0$ mm was the linac entrance. The titanium window was set at $z = 466.5$ mm and the screen station for monitoring the beam profile was at the center of the 6-way duct, which was located at $z = 401.5$ mm.

As the beam traveled through the simulation system, the dynamic properties of the beam at the specified z-positions were observed. Because the accelerating field was a standing-wave RF field, over one cycle, approximately half of the particles traveled in the forward direction and approximately half moved backward. This depended on the phase of the field when entering the field region. Consequently, the continuous electron beam from the gun became a train of electron bunches. The evolution of the dynamic properties of the bunch is shown in Fig. 4a, b. As evident, the electron bunch gained kinetic energy along the linac z-axis, as shown by the increasing graph in Fig. 4a, reaching a final kinetic energy of approximately 4 MeV at the end of the field position. The electron bunch maintained this kinetic energy through the vacuum duct downstream until it reached the titanium window at $z = 401.5$ mm. The ladder-like steps in the field region represent the travel of the bunch across the field boundary between the adjacent cavities. The energy spread of the bunch also increased as the bunch gained higher energy, with the final energy spread on the order of ~ 700 keV as shown in Fig. 4a. The transverse properties of the bunch along z-axis are shown in Fig. 4b. As evident, the bunch had larger transverse size as it traveled down the beamline and the size still increased in the drift space region owing to the transverse momentum and the space-charge effect. The final RMS size was on the order of ~ 1 mm. In contrast to the transverse size, the RMS emittance of the bunch tended to remain unchanged after the end of the field position.

To acquire a complete picture of the bunch at the final position, the bunch distribution in 3D space was plotted along with the bunch's x and y phase spaces. The transverse bunch profile at the titanium window position is shown in Fig. 4c. The RMS transverse size, calculated from all the electrons in the bunch, was 1.5 mm.

The three-dimensional shape of the bunch is shown in Fig. 4d. As evident, the distribution of the electrons in the bunch was more dispersed than in our previous study, wherein the electron beam was generated from the subprogram generator and did not fully represent the actual bunch [29]. The corresponding phase spaces of this electron bunch were similar in both x and y directions, as shown in Fig. 4e, f. At the bunch profile monitoring position (center of the 6-way duct), the characteristic properties of the bunch were similar to those of the final bunch with an RMS beam size of 0.8 ± 0.3 mm. This value was expected when the measurement was performed under these simulated conditions.

To gain a better understanding of the bunch of electrons, the energy spectrum was plotted as shown in Fig. 4g. As evident, the majority of particles in the bunch were captured in the "RF bucket" shown as two large energy peaks at $\sim$ 3.92 MeV and $\sim$ 4.12 MeV. Thus, they experience two stable but separate phase of the field. The particles injected into the field at different phases experience a lower field or even a reverse field and consequently gain lower energy when traveling through the cavities or, in drastic cases, may travel in the reverse direction and are lost in the linac. These minority particles appear as long low-energy tails in the energy spectrum [38]. Consequently, the energy representation of such a bunch can be determined by ignoring low-energy minorities. In our case, the majority of electrons ($\sim 78\%$) had a kinetic energy ≥ 3.9 MeV. According to the explanation above, the bunch energy was calculated as 4.01 ± 0.07 MeV. Note that this energy is slightly greater than the value shown in Fig. 4a, where the values were calculated for all particles in the bunch. Figure 4h illustrates the longitudinal phase space of the bunch. It is clear that most of the particles in the bunch exhibited bunching with a bunch time of $\sim$120 ps. In a typical standing-wave linac, the first cell is normally a half-cell structure with the maximum electric field amplitude at the rear wall of the cell. This results in an electron bunch length of approximately one-fourth the wavelength ($\sim \lambda/4$). In this study, we adopted the longitudinal electric field profile measured using the bead-pull technique, which showed that the field distribution in the first cell was not a half-cell resonant cavity structure. Instead, it appears to be a full-cell resonant cavity structure but with a shorter length than the other four downstream cells, as reported in [27] and [29]. However, we could not confirm this hypothesis because we could not observe the actual inner shape or dimensions of the linac cell cavities. Using this longitudinally measured electric field profile as an input in the ASTRA simulation, the continuous electron beam from the DC gun was bunched with a longitudinal beam distribution, owing to the energy distribution of the RF electric field in the linac cavities. As shown in Fig. 7 of [29], the electron bunch length

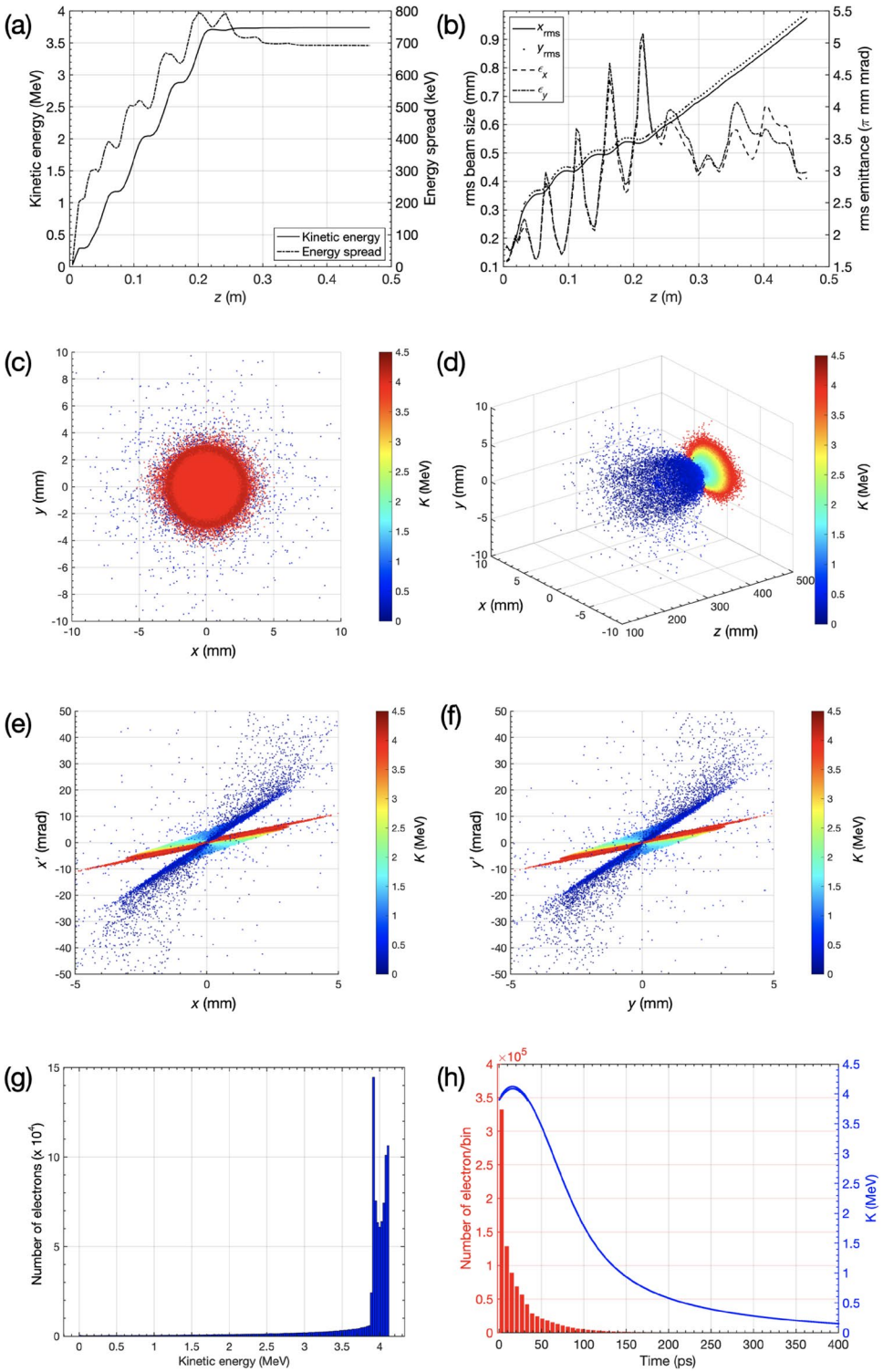

Fig. 4 **a**, **b** Dynamic properties of the electron bunch along the z-axis of the simulation system including the kinetic energy, energy spread, transverse RMS size, and RMS emittance. **c**, **d** Distribution of the electron bunch at the titanium window on the $x - y$ transverse plane and its 3D distribution. **e**, **f** x and y phase spaces. **g** Energy spectrum of the electron bunch at the titanium window. **h** Longitudinal phase space of the same bunch. Note that the red histogram represents number of electrons (macroparticles) and the dark blue dots show the kinetic energy associated with each macroparticle

increased while accelerating through the first cell (with a bunch length of $\sim \lambda/4$) to the third cell (with a bunch length of $\sim \lambda/3 - \lambda/2$), and was almost constant thereafter until the fifth cell. Subsequently, the electron bunch further elongated after exiting the linac's last cavity and traveled in the drift space with a large difference in the energies of the electrons between the head and tail regions, resulting in a bunch length of approximately 120 ps at the position of titanium window (244.5 mm after the linac exit). The total number of macroparticles in the bunch was 909, 557 (corresponding to a total charge of 36 ± 3 pC). This resulted in a peak current of 300 ± 25 mA. However, the average macropulse current is

Table 1 Simulated electron beam parameters at extraction titanium window

Parameter	Value
Electron beam energy (MeV)	4.01 ± 0.07
Bunch length (ps)	~ 120
Bunch charge (pC)	36 ± 3
Bunch current (mA)	300 ± 25
Average current (mA)	106 ± 8
RMS transverse size (mm)	1.5

Table 2 Average beam energy measured in vacuum and in air in comparison with the simulated values

RF peak power (MW)	Gradient (MV/m)	Simulated beam energy (MeV)		Measured average energy (MeV)	
		$E_{k,\text{bunch}}$	$E_{k,\text{head}}$	$E_{k,\text{vacuum}}$	$E_{k,\text{air}}$
1.0	32.1	3.2 ± 0.6	3.48 ± 0.03	2.6 ± 0.2	2.8 ± 0.2
1.2	35.3	3.4 ± 0.7	3.80 ± 0.05	2.8 ± 0.3	3.0 ± 0.3
1.4	38.2	3.8 ± 0.7	4.08 ± 0.08	2.9 ± 0.2	3.4 ± 0.3

more appropriate in practice, and the value estimated based on this calculation was 106 ± 8 mA. Based on our beam dynamics simulation, we obtained important parameters and properties of the electron beam, as summarized in Table 1. These values are for operation under optimal machine conditions and will be an important guideline for future measurement and operation.

Electron beam energy measurements were performed both in the diagnostic chamber (in vacuum) and at a position of 5 cm after the titanium window (in air) using a phosphor screen and a steering magnet installed outside the chamber upstream the diagnostic chamber. The magnetic field distribution of the steering magnet and the calibration curve between the applied electric current and magnetic field amplitude were included in the image processing analysis of the spatial and energy distributions of the electron beam on the phosphor screen using a MATLAB script. When the screen was placed in air at a larger distance, a better energy resolution was achieved. In our preliminary observations, the RF peak power was varied up to 1.4 MW for a complete beam energy measurement at both positions (Table 2). Table 2 shows that the measured average beam energy in air (5 cm after the titanium window) was in line with the simulated beam energy of the entire bunch, with a slightly smaller value. A small difference of 0.4 MeV was consistent for all RF powers and was attributed to energy loss as the beam traveled through the window and ambient air. However, the average energy measured in vacuum had a larger difference owing to the insufficient magnetic field strength (5 mT) of the steering magnet, which resulted in a poorer energy resolution of the diagnostic system at shorter distances. Although the full performance of the machine was limited by certain technical issues, the data in Table 2 can still provide a good understanding of the beam energy measurement. The electron beam current could not be determined because the beam size was larger than the collection area of the Faraday cup installed in the diagnostic chamber. Further improvements to the beam diagnostic system will be made in the future.

4 Monte Carlo simulation of electron beam distribution and electron dose in irradiation section

As mentioned previously, the electron beam produced by our accelerator system was aimed at ambient irradiation. Therefore, the accelerated electron beam must travel from the vacuum to the atmosphere through the titanium window installed at the end of the beam diagnostic section. The electron beam dynamics and properties under ambient conditions are different from those in a vacuum because of the interactions of energetic electrons with air molecules. The two important properties that must be considered for most electron-processing applications are the transverse profile and electron dose along the beam path. In this study, these two properties were estimated using Geant4 software, which calculates the passage of electrons through matter using the Monte Carlo method.

In the simulation setup, the accelerated electron beam properties at the titanium window position acquired from the ASTRA output were converted to the Geant4 format using our MATLAB script and used as an input. This electron beam had an average current of 106 mA with a macropulse length of 1 µs. Note that the dose results were for an electron macropulse and the repetition rate range of this machine was $20 - 200$ Hz. The electron beam was set to traverse a sheet of titanium with a thickness of 50 µm, which is the same as the actual setup. After passing through this titanium window, the electrons were set to travel in air along z-direction, where $z = 0$ cm represents the window exit and $z = 16$ cm represents the final position of the beam (assumed to be the sample position). The setup of the Geant4 simulation is illustrated in Fig. 5. A distance of 16 cm was selected according to the laboratory setup, and the electron beam could not travel farther than this distance because of space limitations. The electron beam properties were measured every 1–2 cm at this distance. Two scorer types: air and B3 film scorers were constructed in the Geant4 simulation to collect the electron doses. The B3 film (> 98% polyvinyl butyral (PVB) and < 2% proprietary Risø National Laboratory

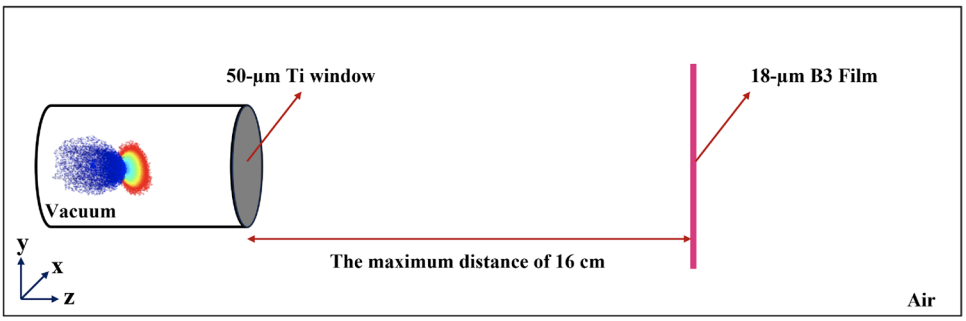

Fig. 5 Schematic of the simulation setup in Geant4 software

pararosaniline radiochromic dye, with a film density of 1.120 g/cm^3, GEX Corp., USA) is a radiochromic material widely used for dose measurements [39]. The volume of air scorer is 20 cm × 20 cm × 40 µm with the bin size of 40 µm × 40 µm × 40 µm while the B3 film scorer volume was set at 20 cm × 20 cm × 18 µm with the bin size of 40 µm × 40 µm × 18 µm. A bin area of 40 µm × 40 µm was implemented because it is the resolution of the scanner used for the exposed film analysis, and the 18-µm thickness was chosen to match the actual film thickness. Because the chemical components in the dye of the real film were not known, we assumed the B3 scorer in the simulation to be a 100% PVB with the same density as that of the real film.

The properties of the electron beam in ambient air at the selected z-positions are shown in Fig. 6. As evident, all the beam profiles were circularly symmetric along the beam path. To determine the root-mean-square transverse width (RMS width; w_{rms}), we adopted the following expression:

$$w_{\mathrm{rms}} = \left[\frac{\int_{-\infty}^{\infty} r^2 f(r)\mathrm{d}r}{\int_{-\infty}^{\infty} f(r)\mathrm{d}r}\right]^{1/2}, \tag{4}$$

where r represents the spatial variables and $f(r)$ is the distribution intensity. In this study, the integration was performed within the limit of $[-3, 3]$ cm, assuming that the distribution intensity was negligible beyond this limit. To obtain

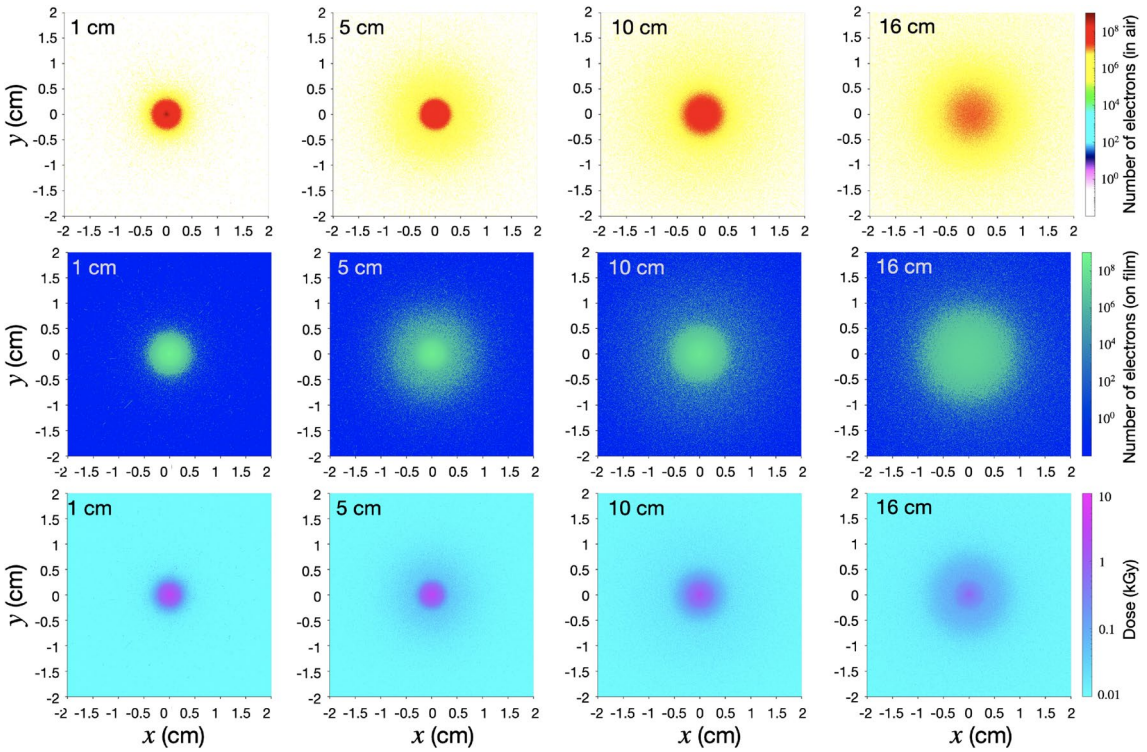

Fig. 6 Selected transverse distributions of electron beam in air (top row), electron beam on B3 film (middle row), and electron deposition dose on B3 film (bottom row) at varied distances along the beam travel distance in ambient atmosphere. Note that the distance from the titanium window is marked at the top-left corner of each map

the statistics, w_{rms} was averaged over the values determined from four cross-sectional planes at angles of 0°, 45°, 90°, and 135° around the z-axis.

The RMS beam widths determined from the three datasets are presented in Fig. 7a. As evident, the RMS beam widths from all the data increased with the traveling distance. Note that the widths calculated from the number of electrons in air and the number of electrons on B3 film changed accordingly, and the values agreed well (with a beam width of approximately 0.6 cm at the final position), indicating that the B3 film did not significantly affect the beam profile and was suitable for beam profile measurements (especially at short distances). In contrast to the first two cases, the beam widths obtained from the dose profile were larger than the values determined from the number of electrons at all distances. This difference was not unexpected because the physical processes are not the same. However, the color of the film was observed in the actual experiment, and the color is related to the electron dose. Therefore, readers must be aware of this discrepancy when adopting the same analysis.

In addition to the transverse profile, the electron deposition dose was estimated from the simulation results. Here, we determined the peak dose, which is the dose value averaged within the square of the area 500 µm × 500 µm centered at the peak, and the average dose, which is the dose averaged within the area defined by the RMS width. The dose values are plotted in Fig. 7b. Both dose values showed similar nonmonotonic variations, with maximum dose value at approximately $z = 2$ cm and then decreased along the distance. The dose values were in the range of $1 - 5$ kGy, which is within the range for the B3 film [39]. The peak doses were higher than the average doses, indicating that the dose was higher at the center of the beam. At short distances ($1 - 8$ cm), the peak doses were higher than the average doses compared with the long distance (> 8 cm), indicating high nonuniformity of both the transverse electron density and deposition dose. As the beam traveled further, this peak density was smeared off, and the peak and average doses converged, indicating that the deposition area was more uniform.

As presented in Fig. 7b, the calculated electron dose in air decreases very quickly after a distance of 5 cm from the titanium window. Therefore, we set this distance as the experimental limit and performed preliminary dose measurements at this position. Dose measurements in air using a GEX B3 dosimeter were carried out as reported by [40]. The spatial dose distribution on the B3 film shows a circular area with a diameter of 1.5 cm, which is in good agreement with the simulated spatial dose distribution shown in Fig. 6. The measured dose rate of 6 kGy/min is close to the simulated maximum dose of 5 kGy. In addition, dose measurements using a water phantom were also performed by irradiating an electron beam of energy approximately $3.4 - 4.0$ MeV

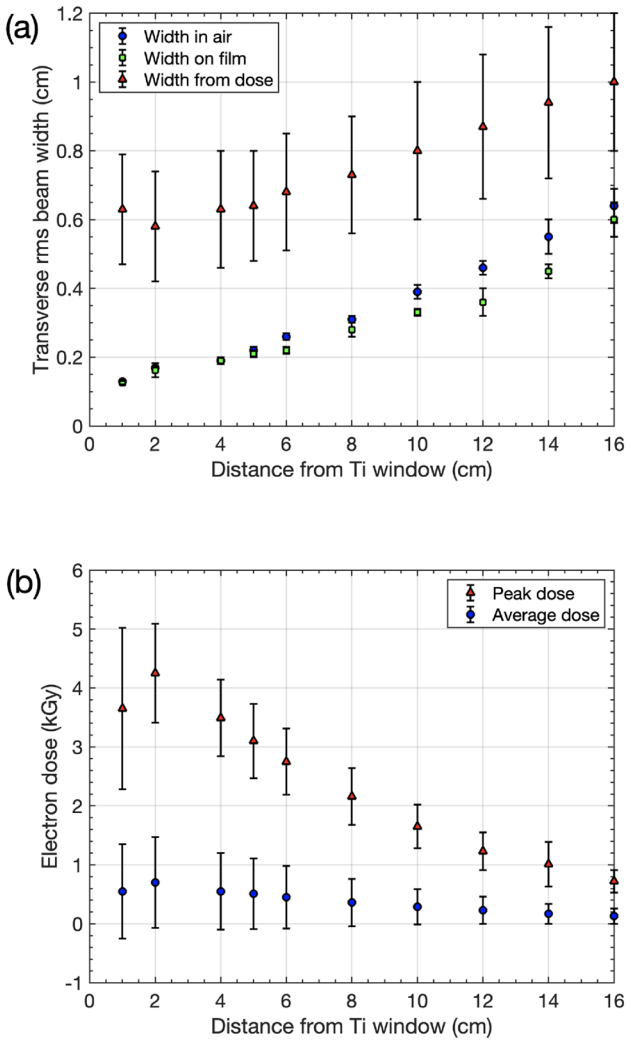

Fig. 7 **a** Transverse electron beam widths in ambient calculated from number of electrons in air, number of electrons on B3 film, and electron dose along the beam path. **b** Electron dose around the peak and average doses along the beam path

through a water column with varying water depths from $0.5 - 2.0$ cm while the B3 film was placed below the water at a fixed distance of 5.0 cm from the window [41]. For a better illustration and comparison, we replotted the measurement results and the Geant4 simulation using ASTRA beam distribution as the input with a corresponding beam energy of 2.94 MeV (Fig. 8). It was found that the maximum water depth that the electron beam could penetrate was approximately 1.5 cm. The experiments were conducted and analyzed using two sets of calibrations specified by code numbers 1 and 2 in the plot. Code 1 refers to a default usable range calibration provided by the RisøScan Dosimetry Software, which is compatible with B3 film, whereas code 2 refers to an in-house calibration. We believe these results provide useful guidelines for many activities, such as the estimation of irradiation dose, sample exposure area

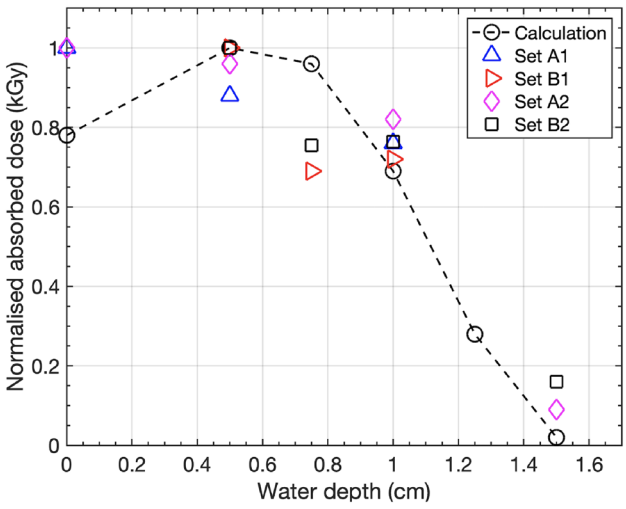

Fig. 8 Normalized absorbed dose in water compared with the Geant4 calculation. Set A indicates the experimental samples with set B for stability verification at particular water depths. Code 1 and 2 are specified for different calibration procedures. The figure is replotted from [41]

optimization, and the machine's future design, for example, a beam sweeper.

5 Conclusion

The reengineering of a 4 MeV electron medical linac for electron beam irradiation applications is under process at the PBP-CMU Electron Linac Laboratory in Thailand. Modifications have been performed, and guidelines for the beam properties are required. The emission of electrons from the cathode was calculated based on the thermionic emission theory to serve as the input for generating a more realistic electron beam from the electron gun using CST Studio Suite® software. The simulated beam with an average kinetic energy of approximately 17 keV was then used as the input to study the electron beam dynamics in the accelerating section using the ASTRA code. At the maximum RF accelerating gradient of 37.5 MV/m, a circular electron beam with a final average kinetic energy of approximately 4 MeV can be produced with an average current on the order of 100 mA and an average transverse beam size of approximately 1.5 mm at the extraction window situated at the end position of the system. After the beam exited the window to the ambient environment, the transverse beam profile and deposition dose along the beam path were calculated using Geant4 software. The results showed an increase in the beam size and a decrease in the electron dose with the traveling distance. The dose values were in the range of $1-5$ kGy based on our beam properties and simulation scope. These values agreed well with our preliminary measurements and will be important guidelines for further reengineering steps, including other practical activities, such as electron beam characterization, electron dose measurement, and irradiation condition design.

In addition to the advantage of a considerably lower cost, when compared with the existing state-of-the-art electron irradiation machines, this modified electron linac system offered the possibility for beam energy adjustment in a wide range of $0.6-4$ MeV. This provides more flexibility on irradiation applications with different desired electron beam energy. This is rarely observed in other electron beam irradiation systems, particularly those modified from the old medical linac system for similar application purposes [42, 43] or newly developed electron linac systems using design and simulation methods similar to our technique, but with less detailed study and simulation results than those presented in this study [44, 45]. Moreover, the installation of the diagnostic chamber facilitated a detailed characterization of the electron beam properties before exiting the ambient air. With the aid of Monte Carlo simulations, an accurate calculation of the electron dose distribution at specific locations was obtained. This is crucial to ensure that the desired radiation dose is delivered to the samples in the actual experiments.

Acknowledgements The authors acknowledge the collaborative support for the simulation provided by the High-Performance Computing (HPC) cluster of the National Astronomical Research Institute of Thailand (NARIT). The authors are deeply grateful to Pitch Wongkummoon for providing data and analyzing the electron dose measurements. MJ thanks the CMU postdoctoral presidential scholarship (2019–2020) for its financial support.

Declarations

Conflict of interest The authors declare that they have no conflict of interest.

References

1. M.S. Wkeglowski, S. Błacha, A. Phillips, Electron beam welding-techniques and trends-review. Vacuum **130**, 72–92 (2016). https://doi.org/10.1016/j.vacuum.2016.05.004
2. U. Henniges, M. Hasani, A. Potthast et al., Electron beam irradiation of cellulosic materials-opportunities and limitations. Materials **6**, 1584–1598 (2013). https://doi.org/10.3390/ma6051584
3. Y. Chen, Nanofabrication by electron beam lithography and its applications: a review. Microelectron. Eng. **135**, 57–72 (2015). https://doi.org/10.1016/j.mee.2015.02.042
4. I.G. Gonzalez-Martinez, A. Bachmatiuk, V. Bezugly et al., Electron-beam induced synthesis of nanostructures: a review. Nanoscale **8**, 11340–11362 (2016). https://doi.org/10.1039/C6NR01941B
5. I. Jang, S.B. Sinnott, D. Danailov et al., Molecular dynamics simulation study of carbon nanotube welding under electron beam irradiation. Nano Lett. **4**, 109–114 (2004). https://doi.org/10.1021/nl034946t

6. R. Bhat, K.R. Sridhar, Nutritional quality evaluation of electron beam-irradiated lotus (*Nelumbo nucifera*) seeds. Food Chem. **107**, 174–184 (2008). https://doi.org/10.1016/j.foodchem.2007.08.002
7. A.G. Chmielewski, M. Haji-Saeid, S. Ahmed, Progress in radiation processing of polymers. Nucl. Instrum. Methods Phys. Res. B **236**, 44–54 (2005). https://doi.org/10.1016/j.nimb.2005.03.247
8. D. Auhl, J. Stange, H. Münstedt et al., Long-chain branched polypropylenes by electron beam irradiation and their rheological properties. Macromolecules **37**, 9465–9472 (2004). https://doi.org/10.1021/ma030579w
9. D.J. Leonard, L.T. Pick, D.F. Farrar et al., The modification of PLA and PLGA using electron-beam radiation. J. Biomed. Mater. Res. A **89**, 567–574 (2009). https://doi.org/10.1002/jbm.a.31998
10. K. Lunkwitz, U. Lappan, D. Lehmann, Modification of fluoropolymers by means of electron beam irradiation. Radiat. Phys. Chem. **57**, 373–376 (2000). https://doi.org/10.1016/S0969-806X(99)00407-7
11. M.M. Nasef, H. Saidi, K.Z.M. Dahlan, Electron beam irradiation effects on ethylene-tetrafluoroethylene copolymer films. Radiat. Phys. Chem. **68**, 875–883 (2003). https://doi.org/10.1016/S0969-806X(03)00209-3
12. Y. Liu, X. Huang, J. Liu et al., Structure and tensile properties of carbon fibers based on electron-beam irradiated polyacrylonitrile fibers. J. Mater. Sci. (2020). https://doi.org/10.1007/s10853-019-04182-4
13. A. Iuliano, M. Nowacka, K. Rybak et al., The effects of electron beam radiation on material properties and degradation of commercial PBAT/PLA blend. J. Appl. Polym. Sci. **137**, 48462 (2020). https://doi.org/10.1002/app.48462
14. M. Driscoll, A. Stipanovic, W. Winter et al., Electron beam irradiation of cellulose. Radiat. Phys. Chem. **78**, 539–542 (2009). https://doi.org/10.1016/j.radphyschem.2009.03.080
15. T. Sasuga, N. Hayakawa, K. Yoshida et al., Degradation in tensile properties of aromatic polymers by electron beam irradiation. Polymer **26**, 1039–1045 (1985). https://doi.org/10.1016/0032-3861(85)90226-5
16. A.V. Krasheninnikov, F.J.N.M. Banhart, Engineering of nanostructured carbon materials with electron or ion beams. Nat. Mater. **6**, 723–733 (2007). https://doi.org/10.1038/nmat1996
17. H. Malekpour, P. Ramnani, S. Srinivasan et al., Thermal conductivity of graphene with defects induced by electron beam irradiation. Nanoscale **8**, 14608–14616 (2016). https://doi.org/10.1039/C6NR03470E
18. E. Barsotti, S.P. Tan, L. Goual et al., Amorphization of carbon nanotubes in water by electron beam radiation. Carbon **156**, 313–319 (2020). https://doi.org/10.1016/j.carbon.2019.09.043
19. I. Childres, L.A. Jauregui, M. Foxe et al., Effect of electron-beam irradiation on graphene field effect devices. Appl. Phys. Lett. **97**, 173109 (2010). https://doi.org/10.1063/1.3502610
20. M.Z. Iqbal, N. Anwar, S. Siddique et al., Formation of pn-junction with stable n-doping in graphene field effect transistors using e-beam irradiation. Opt. Mater. **69**, 254–258 (2017). https://doi.org/10.1016/j.optmat.2017.04.041
21. F. Giubileo, A. Di Bartolomeo, N. Martucciello et al., Contact resistance and channel conductance of graphene field-effect transistors under low-energy electron irradiation. Nanomaterials **6**, 206 (2016). https://doi.org/10.3390/nano6110206
22. F. Banhart, The formation of a connection between carbon nanotubes in an electron beam. Nano Lett. **1**, 329–332 (2001). https://doi.org/10.1021/nl015541g
23. J. Li, F. Banhart, The engineering of hot carbon nanotubes with a focused electron beam. Nano Lett. **4**, 1143–1146 (2004). https://doi.org/10.1021/nl049705f
24. A. Kis, G. Csanyi, J.P. Salvetat et al., Reinforcement of single-walled carbon nanotube bundles by intertube bridging. Nat. Mater. **3**, 153–157 (2004). https://doi.org/10.1038/nmat1076
25. F. Bouzarjomehri, V. Dad, B. Hajimohammadi et al., The effect of electron-beam irradiation on microbiological properties and sensory characteristics of sausages. Radiat. Phys. Chem. **168**, 108524 (2020). https://doi.org/10.1016/j.radphyschem.2019.108524
26. G. Craciun, E. Manaila, M.D. Stelescu, New elastomeric materials based on natural rubber obtained by electron beam irradiation for food and pharmaceutical use. Materials **9**, 999 (2016). https://doi.org/10.3390/ma9120999
27. S. Rimjaem, E. Kongmon, M.W. Rhodes et al., Electron linear accelerator system for natural rubber vulcanization. Nucl. Instrum. Methods Phys. Res. B **406**, 233–238 (2017). https://doi.org/10.1016/j.nimb.2016.11.016
28. W. Jansomboon, S. Loykulnant, P. Kongkachuichay et al., Electron beam radiation curing of natural rubber filled with silica-graphene mixture prepared by latex mixing. Ind. Crops Prod. **141**, 111789 (2019). https://doi.org/10.1016/j.indcrop.2019.111789
29. P. Apiwattanakul, S. Rimjaem, Electron beam dynamic study and Monte Carlo simulation of accelerator-based irradiation system for natural rubber vulcanization. Nucl. Instrum. Methods Phys. Res. B **466**, 69–75 (2020). https://doi.org/10.1016/j.nimb.2020.01.012
30. Mitsubishi Electric Co., Instruction manual of medical linear accelerator model ML-4M (1984)
31. J.L. Cronin, Modern dispenser cathodes. In: IEEE Proceedings **128**, 19–32 (1981)
32. E.L. Murphy, R. Good Jr., Thermionic emission, field emission, and the transition region. Phys. Rev. **102**, 1464 (1956). https://doi.org/10.1103/PhysRev.102.1464
33. C. Herring, M. Nichols, Thermionic emission. Rev. Mod. Phys. **21**, 185 (1949). https://doi.org/10.1103/RevModPhys.21.185
34. R. Longo, Physics of thermionic dispenser cathode aging. J. Appl. Phys. **94**, 6966–6975 (2003). https://doi.org/10.1063/1.1621728
35. M. Kiziroglou, X. Li, A.A. Zhukov et al., Thermionic field emission at electrodeposited Ni-Si Schottky barriers. Solid State Electron. **52**, 1032–1038 (2008). https://doi.org/10.1016/j.sse.2008.03.002
36. C. Crowell, The Richardson constant for thermionic emission in Schottky barrier diodes. Solid-State Electron. **8**, 395–399 (1965)
37. CST Studio Suit®. CST – Dassault Systemes Deutschland GmbH, Germany (2023)
38. J. St Aubin, Three dimensional simulation and magnetic decoupling of the linac in a linac-mr system. Ph.D. thesis, University of Alberta (2010)
39. R. Chilkulwar, S. Sharma, N. Chaudhary et al., Dosimetric evaluation of an indigenously developed 10 MeV industrial electron beam irradiator. Radiat. Meas. **47**, 628–663 (2012). https://doi.org/10.1016/j.radmeas.2012.06.009
40. C. Thongbai, S. Rimjaem, J. Saisut et al., in: 13th international particle accelerator conference (IPAC2022), Present status of linear accelerator system for natural rubber vulcanization at Chiang Mai University. JACOW Publishing, Geneva, Switzerland, (2022), pp 3057–3060. https://doi.org/10.18429/JACoW-IPAC2022-THPOMS040
41. P. Wongkummoon, C. Thongbai, J. Saisut et al., in 13th international particle accelerator conference (IPAC2022) Design and parameterization of electron beam irradiation system for natural rubber vulcanization. JACOW Publishing, Geneva, Switzerland, 2022, pp 3061–3063. https://doi.org/10.18429/JACoWIPAC2022-THPOMS041
42. J.I.M. Botman, A.T.A.M. Derksen, A.M. Van Herk et al., A linear accelerator as a tool for investigations into free radical polymerization kinetics and mechanisms by means of pulsed electron beam polymerization. Nucl. Instrum. Methods Phys. Res. B **139**, 490–494 (1998). https://doi.org/10.1016/S0168-583X(97)00948-8
43. W. Van Duijneveldt, J.I.M. Botman, C.J. Timmermans et al., Modification of a medical linac to a polymer irradiation facility.

Nucl. Instrum. Methods Phys. Res. B **79**, 871–874 (1993). https://doi.org/10.1016/0168-583X(93)95488-Q
44. L. Auditore, R.C. Barna, D. De Pasquale et al., Pulsed 5 MeV standing wave electron linac for radiation processing. Phys. Rev. ST Accel. Beams **7**, 030101 (2004). https://doi.org/10.1103/PhysRevSTAB.7.030101
45. S. Chunjarean, K. Manasatitpong, N. Yachum et al., in Journal Physics Conference Series, Development of a 6 MeV electron beam energy linac for fruit sterilization. Vol. 2431, IOP Publishing, (2023), p 012071. https://doi.org/10.1088/1742-6596/2431/1/012071

Authors and Affiliations

Monchai Jitvisate[1,4] · Pittaya Apiwattanakul[1] · Noppadol Kangrang[1,2] · Jatuporn Saisut[1,2,3] · Chitrlada Thongbai[1,2,3] · Sakhorn Rimjaem[1,2,3]

✉ Sakhorn Rimjaem
sakhorn.rimjaem@cmu.ac.th

[1] PBP-CMU Electron Linac Laboratory, Department of Physics and Materials Science, Plasma and Beam Physics Research Facility, Faculty of Science, Chiang Mai University, Chiang Mai 50200, Thailand

[2] Research Unit for Development and Utilization of Electron Linear Accelerator and Ultrafast Infrared/Terahertz Laser, Chiang Mai University, Chiang Mai 50200, Thailand

[3] Thailand Center of Excellence in Physics, Ministry of Higher Education, Science, Research and Innovation, Bangkok 10400, Thailand

[4] Present Address: School of Physics, Institute of Science, Suranaree University of Technology, Nakhon Ratchasima 30000, Thailand